This article has been accepted for publication in IEEE Open Journal of Antennas and Propagation. This is the author's version which has not been fully edited and content may change prior to final publication. Citation information: DOI 10.1109/OJAP.2024.3392628

IEEE Open Journal of Antennas and Propagation

Received XX Month XXXX; revised X Month XXXX; accepted XX Month XXXX.

Fully Embedded Dual-Element Dielectric-Based Antenna for Sub-and Terahertz Applications

EHSAN RAHMATI[1], Member, IEEE, PASCAL BURASA[1], Member, IEEE, ELHAM BALADI[1], Member, IEEE, AND MOHAMMAD S. SHARAWI[2], Fellow, IEEE

[1]Department of Electrical Engineering, École Polytechnique de Montréal, University of Montreal, Montreal, QC H3T 1J4, Canada
[2]Blue Origin LLC, Kent, WA, 98032 USA

CORRESPONDING AUTHOR: E. Rahmati (e-mail: ehsan.rahmati@polymtl.ca).

This work was partially funded by the Natural Sciences and Engineering Research Council of Canada (NSERC), under the New Frontiers in Research Fund (NFRF) with project number NFRFE-2020-00355.

ABSTRACT A completely embedded, planar, dual-element dielectric based antenna directly fed by a substrate integrated insulated guide within the same layer in Sub-THz band is presented in this paper. A dielectric layer is employed to make the structure stable. The proposed structure is compatible with the standard planar millimeter-wave and terahertz manufacturing technologies. To minimize the reflection loss, matching air holes inside the guiding channel of the waveguide and air holes with a smaller perforation radius surrounding the antenna are created. The proposed compact antenna, which has been successfully tested, covers the frequency range of 234.5-278.1 GHz with a measured impedance bandwidth of 17.01%, a proper simulated average radiation efficiency of 93.6%, and a maximum gain as well as average gain of 16.08 dBi and 12.56 dBi from measurement results, respectively. Because of these features, the suggested antenna would be a great candidate for short-range wireless applications in Sub-THz frequency bands.

INDEX TERMS Dielectric-based antenna, dielectric resonator antenna, substrate integrated insulated guide, Terahertz (THz), wideband antenna.

I. INTRODUCTION

TERAHERTZ (THz) frequency bands can provide the required vast spectrum for new applications that need high data rates in 6G wireless systems, such as the distribution of wireless data at high speed, wireless cognition, sensing, and the Internet of Everything (IoE) [1], [2], [3]. Additionally, the capabilities of high spatial resolution and proper penetration depth with nonionizing radiation properties make these frequency bands a highly desirable choice for imaging systems [3],[4]. However, wireless communications in these frequency bands pose a greater challenge due to the presence of high propagation path loss, imprecise fabrication of the antennas, and atmospheric attenuation [5], [6]. Therefore, meeting the requirements of future wireless systems requires the development of high gain and wideband antennas [7], [8], [9].

Numerous antenna designs have been reported to improve antenna performance in Sub-THz and THz frequency bands, such as a leaky wave waveguide-fed THz antenna based on a dielectric lens structure [10], THz horn antennas [9], reflectarray antennas [11], THz photoconductive antennas based on a defective photonic crystal substrate [12], [13], and Fabry–Perot cavity antennas [14]. The integration of conventional lens and horn antennas with other planar devices is challenging due to their bulky size and non-planar form [15], [8]. Therefore, to realize compact-integrated systems operating at THz frequencies, antenna development in planar form is necessary [8]. On-chip antennas realized in the standard metal-oxide semiconductor (CMOS) process are good candidates for the integration from a fabrication standpoint. However, they suffer from poor radiation efficiency and low gain characteristics [4], [16], [17]. A dielectric resonator antenna (DRA) possesses the advantageous characteristics of low loss, easy integration with other components, high gain, and small size, making it a suitable solution for improving the antenna performance in the THz regime [18], [19], [20], [21].

To develop a compact antenna with the capability of integration with other devices, a feeding mechanism in planar form is needed [22]. Substrate integrated waveguide (SIW) structures based on a planar technique exhibit compatibility with both standard printed circuit board (PCB) as well as low-temperature co-fired ceramic (LTCC) fabrication technologies [23]. However, the antenna fabrication using SIW technology for frequencies above 200 GHz is considerably intricate and costly due to the metallization of tiny vias [24]. Dielectric waveguides of planar geometry, such as substrate-on-glass (SOG) dielectric waveguides and substrate integrated image-

This work is licensed under a Creative Commons Attribution 4.0 License. For more information, see https://creativecommons.org/licenses/by/4.0/

This work is licensed under a Creative Commons Attribution-NonCommercial-NoDerivatives 4.0 License. For more information, see https://creativecommons.org/licenses/by-nc-nd/4

This article has been accepted for publication in IEEE Open Journal of Antennas and Propagation. This is the author's version which has not been fully edited and content may change prior to final publication. Citation information: DOI 10.1109/OJAP.2024.3392628

guides (SIIGs), are suitable for being employed as feeding networks in the millimeter wave (mmW) and THz integrated circuits where the waveguide transmission losses are determined by the dielectric losses [22], [25], [26]. Some works were conducted to integrate a cylindrical DRA and a photonic crystal waveguide in THz frequency band for end-fire radiation [27] and [28]. In [27], for example, an integrated DRA based on SOG technology showed an impedance bandwidth of 5.2% in the frequency range of 317 to 334 GHz. In [28], a topological photonic crystal waveguide showed a low transmission loss. However, the proposed structure needs many perforation air holes in comparison with the structure reported in [27], and is suffering from lack of a needed supporting substrate due to the thin and fragile silicon wafer at THz band.

In this work, an integrated dual-element dielectric-based antenna concept with a substrate integrated insulated guide as the feeding structure is presented for Sub-and THz bands for the first time. Most of the reported substrate integrated DRAs in the literature operate at Sub 100 GHz frequencies [29], [30]. They are made up of two parts, namely a substrate integrated DRA and a feeding structure, which are often not implemented within the same layer, and their designs are compatible with the conventional microwave and Sub 100 GHz manufacturing technologies. Therefore, from the fabrication perspective, they are not practical for application in the THz frequency range due to errors resulted from the assembly process and manufacturing techniques such as metallization of tiny vias for frequencies above 200 GHz [24]. Additionally, the conduction (ohmic) losses are crucial at the THz band, thereby limiting the employed feeding methods such as microstrip line and substrate integrated waveguide (SIW) technologies [22], [31]. Here, we proposed a fully embedded dielectric antenna, which is fed directly by the substrate integrated dielectric guide within the same (substrate) layer. The employed feeding method is implemented within the substrate integrated circuit technology, which is compatible with standard planar millimeter-wave (mmW)/Terahertz (THz) manufacturing technologies [31], [32], [33]. It is worthwhile to note that for the sake of proof of concept, alumina has been used in this work. However, the proposed solution can be used at a higher end of the THz band with low loss materials such as silicon based on deep reactive ion-etching (DRIE) [25] and has the capability of hybrid integration with various waveguide structures on the same substrate [31] and [33]. Furthermore, an air-gap is created between the guiding channel (the alumina layer) and the ground (metal) plane of the proposed antenna, resulting in not only lower transmission losses (due to the decrease in waveguide attenuation) but also antenna gain enhancement based on the image theory. The proposed antenna brings the benefits of small size, simple design, wide bandwidth, high gain, high radiation efficiency, and completely embedded design in a waveguide system with the capability of easy integration in the mmW or THz systems.

This paper is organized as follows: The design principles, the substrate integrated insulated waveguide as a feeding mechanism, and the antenna structure are presented in detail in Section II. Section III compares the simulated and the measured results. Finally, the conclusion is drawn in Section IV.

II. DUAL-ELEMENT DRA OPERATING PRINCIPLES

The proposed antenna structure consists of three main parts, namely a fully-embedded dual-element dielectric antenna, substrate integrated insulated guides, and an electric wall. The dual-element DRA is fed directly by planar dielectric waveguides operating in E^{Z}_{11} mode. By considering the field distribution similarity between the propagating mode in the waveguide and the $HEM_{11\delta}$ mode of the cylindrical dielectric resonator, it is expected that the proposed waveguide can excite the dielectric resonator mode, and therefore, broadside radiation patterns can be achieved. In this section, the proposed waveguide that forms the feeding mechanism and antenna configuration are presented, and a bandwidth study is also performed.

A. FEEDING MECHANISM

To feed the dual-element DRA, we introduce a substrate integrated insulated waveguide in the frequency range of 220-280 GHz. It is constructed by creating symmetric air-hole-perforated sections in a triangular lattice on both sides of an alumina guiding channel with a relative permittivity of 9.8 and tanδ=0.001, where the substrate is supported by a metal coated RO4003 layer with a permittivity of 3.55 and tanδ=0.0027, as shown in Fig.1. The perforated sections decrease the effective dielectric constant of the alumina substrate. Therefore, this structure operates based on a total internal reflection mechanism similar to substrate integrated image guide [31], [33], where the guiding mechanism is provided due to the

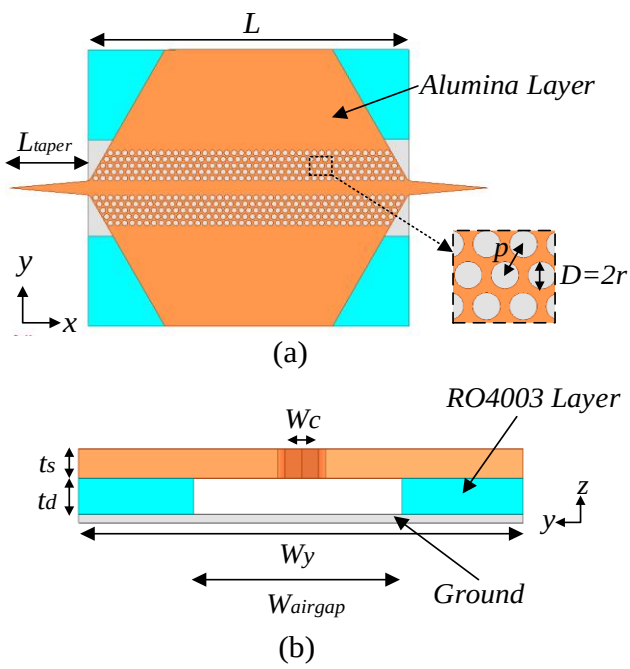

FIGURE 1. **The designed substrate integrated insulated guide, a) Top view and (b) Side view**.

This work is licensed under a Creative Commons Attribution-NonCommercial-NoDerivatives 4.0 License. For more information, see https://creativecommons.org/licenses/by-nc-nd/4

This article has been accepted for publication in IEEE Open Journal of Antennas and Propagation. This is the author's version which has not been fully edited and content may change prior to final publication. Citation information: DOI 10.1109/OJAP.2024.3392628

difference between the dielectric constants of the alumina guiding channel and perforated sections as well as index confinement in the vertical direction. The transition between the waveguide and WR3 rectangular waveguides, used for measurement purposes, is facilitated by the utilization of two tapered channel waveguides, as illustrated in Fig. 1. Additionally, an air gap is created between the alumina layer and the ground plane. As shown in Fig. 1(b), the RO4003 layer of light blue color implemented at two sides of the guiding channel supports alumina layer. The radius and lattice constant of the air hole perforation created using laser micromachining are r = 0.1 mm and p = 0.264 mm, respectively. The optimization process is performed through CST Microwave Studio v2021. The optimized parameters used in the design are: the width of the guiding channel W_c= 0.258 mm, the thickness of the alumina layer t_s=0.254 mm, the thickness of the RO4003 layer t_d= 0.305 mm, the width of the air gap W_{airgap}= 3.5 mm, and the length of the taper L_{taper}= 2.86 mm. The designed waveguide is depicted in Fig. 1. It should be highlighted that the dimensional parameters are optimized to design a waveguide operating in its fundamental propagation mode, to achieve a proper transmission, and to prevent the bandgap effect resulting from the Bragg condition [31].

To fabricate the presented waveguide, laser micromachining technology is employed to create the perforation of air holes. The ultimate design is chosen by taking into account the manufacturing limitations of laser drilling systems. The S-parameters were measured using an Agilent Network Analyzer (PNA-X N5247A). The simulated and measured results of the designed waveguide are shown in Fig. 2(a). The discrepancies between simulated and measured results can be attributed to materials and fabrication tolerances. Additionally, the propagating field at 250 GHz, i.e., at the center frequency, is confined inside the alumina guiding channel possessing a high permittivity, as shown in Fig. 2(b) and (c). The designed waveguide is then employed as a feeding mechanism for the proposed dual-element DRA as discussed in the next section.

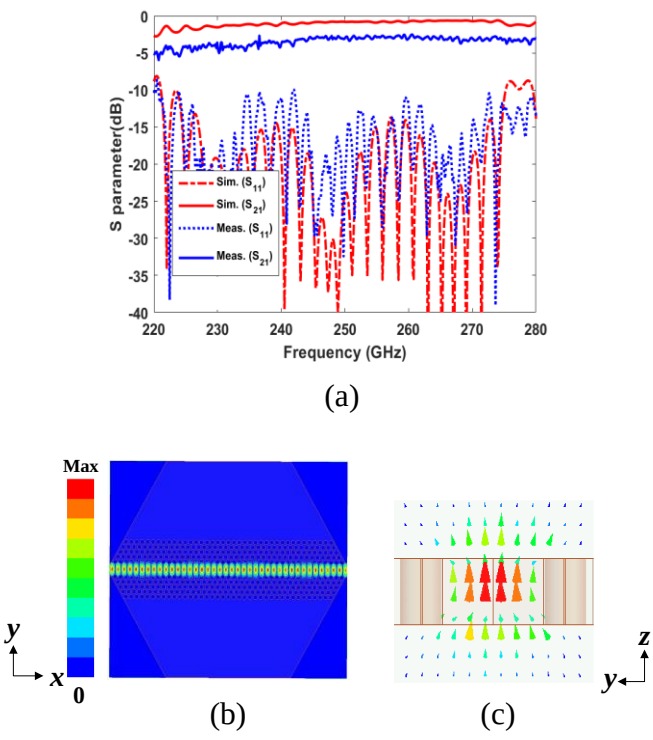

FIGURE 2. (a) Simulated and measured S-parameters of the proposed waveguide, (b) magnitude of the electric field distribution at 250 GHz (top view), and (c) magnitude of the electric field distribution at 250 GHz (cross-sectional view).

B. ANTENNA CONFIGURATION

Figure. 3 shows the configuration of the proposed dual-element DRA. The proposed dual-element DRA comprises two identical dielectric antennas, which are completely embedded inside the alumina guiding channel of the waveguide on two sides of an aluminum wall. The aluminum wall has been integrated between the two main antennas (two main radiating elements) to avoid any potential internal coupling that may occur between the two ports. A differential feeding mechanism, wherein two excitation ports of the antenna are out of phase and have the same magnitude, is employed to feed the dual-element DRA.

To achieve high gain and proper radiation patterns, the thickness of the RO4003 layer t_d= 0.305 mm is chosen based on image theory. The feeding waveguide mechanism and dimensions are the same as the waveguide presented in the previous section. The dimensions of the aluminium wall, namely the width (W_m= 0.254 mm) and length (L_m= 7 mm), have been taken into consideration with respect to the feasibility of fabrication in our Poly-Grames Center at Polytechnique Montréal. The width (W) and length (L) of the whole structure are 10.7 mm and 10 mm, respectively. To improve the impedance bandwidth, air holes having a radius of r_2 on both sides of the guiding channel and matching air holes with a radius and distance of $r_{matching}$ and $d_{matching}$ inside the guiding channels are created. Additionally, four air holes are removed on both sides of the alumina guiding channel. As can be observed in Fig. 4, the created elements on both sides of each individual alumina guiding channel are non-radiating elements since the field distributions is concentrated only inside two central elements. In fact, they contribute to enhance the impedance matching and most of the radiation contribution originates from the dual-element DRA created inside the guiding channel. In addition, H-field and E-field distributions of the dual-element DRA shown in this figure confirm the excitation of the HEM11δ mode of the antenna. The first and second coefficient numbers in 2x1y and 2x3y in the caption of Fig. 3 designate the number of elements along the x-axis and the y-axis, respectively.

C. BANDWIDTH STUDY

Here, we analyze the effect of radius (r_2), the matching air holes, and four non-radiating elements on the impedance matching bandwidth with -10 dB matching criteria. Then, the

This work is licensed under a Creative Commons Attribution-NonCommercial-NoDerivatives 4.0 License. For more information, see https://creativecommons.org/licenses/by-nc-nd/4

This article has been accepted for publication in IEEE Open Journal of Antennas and Propagation. This is the author's version which has not been fully edited and content may change prior to final publication. Citation information: DOI 10.1109/OJAP.2024.3392628

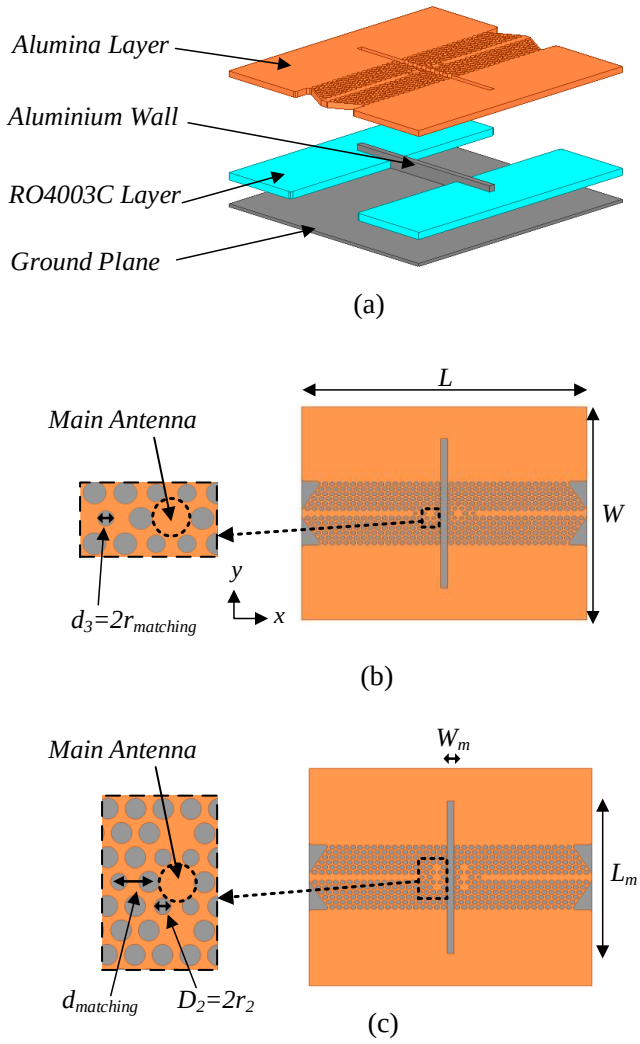

FIGURE 3. Geometry of the proposed dual-element dielectric based antenna (a) Dimetric view, (b) 2x1y configuration (top view), and (c) 2x3y configuration (top view), when the diameter of the main antenna is 0.329 mm.

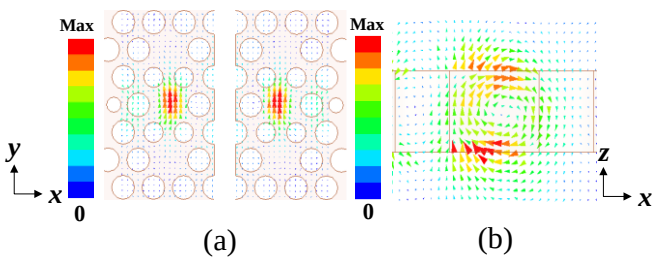

FIGURE 4. H-field and E-field distributions of the dual-element DRA for 2x3y configuration from (a) Top view (*XY* plane) and (b) Cross-sectional view (*XZ* plane), respectively.

antenna performance for two different configurations of 2x1y and 2x3y is investigated.

First, the reflection coefficient of the DRA for the (2x1y) configuration without using the matching air holes is plotted versus frequency for various r_2 dimensions (0.06 mm, 0.085 mm, and 0.1 mm) in Fig. 5 (a). With reference to this figure, when r_2 increases from 0.06 mm to 0.1 mm, -10 dB impedance bandwidth of the antenna shifts upwards with an increase in r_2 and the magnitude of the reflection coefficient is increased at lower frequencies. It can be inferred from this data that the reduction of the DRA dimension, and as a result, the upshift of the antenna resonance frequency is responsible for the observed decrease in the impedance bandwidth [18]. The observed ripple and several minima in the reflection coefficient of the developed antenna are caused by the reflected waves between the proposed waveguide, the radiating elements, and the aluminum wall. In addition, matching air hole is used for a purpose of improving the impedance matching, which is in agreement with coupling mode theory [27]. For the sake of brevity, the reflection coefficient of the DRA without employing the matching air holes is presented and compared to that of the DRA with employing the matching air holes whose dimensions have previously been optimized ($r_{matching}$= 0.0635 mm and $d_{matching}$=0.214 mm). The simulation results shown in Fig. 5 (b) demonstrate the improved matching for the case of the DRA with the matching air hole. The final dimensions of the proposed structure are specified in Table 1.

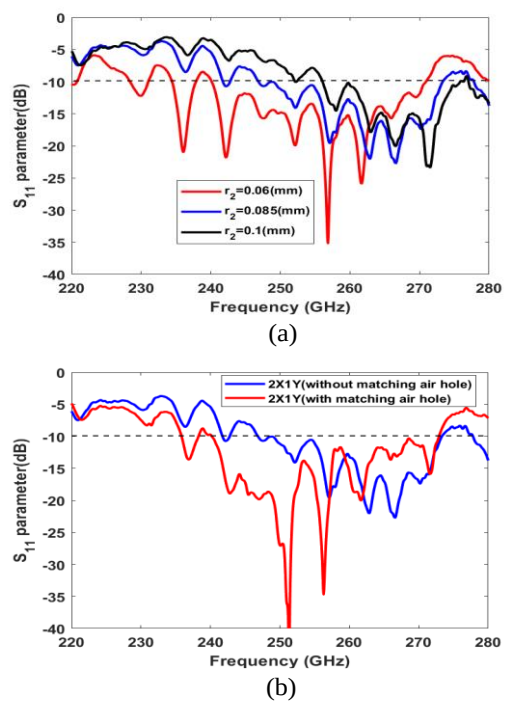

FIGURE 5. (a) Simulated S_{11} parameter for the (2x1y) configuration of the DRA for various r_2 dimensions and (b) Study of the air hole matching effect on S_{11} parameter for the (2x1y) configuration of the DRA.

This work is licensed under a Creative Commons Attribution-NonCommercial-NoDerivatives 4.0 License. For more information, see https://creativecommons.org/licenses/by-nc-nd/4

This article has been accepted for publication in IEEE Open Journal of Antennas and Propagation. This is the author's version which has not been fully edited and content may change prior to final publication. Citation information: DOI 10.1109/OJAP.2024.3392628

TABLE 1. Parameters of the proposed antenna

Parameter	Value (in mm)	Parameter	Value (in mm)
p	0.264	r_2	0.085
r	0.1	W_m	0.254
t_s	0.254	L_m	7
t_d	0.305	L	10
L_{taper}	2.86	W	10.7
$d_{matching}$	0.214	$r_{matching}$	0.0635
W_{airgap}	3.5	W_c	0.258

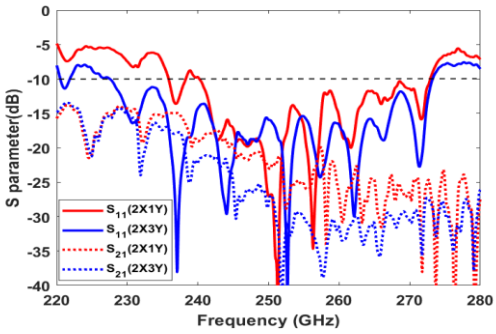

FIGURE 6. Simulated S parameters of the designed DRA for (2x1y) and (2x3y) configurations.

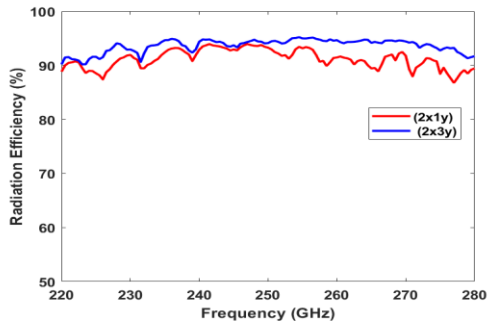

FIGURE 7. Simulated radiation efficiency for two different configurations of (2x1y) and (2x3y).

Similarly, the obtained results shown in Fig. 6 exhibit the decrease in the reflection coefficient for the antenna configuration (2x 3y) in comparison to the (2x1y), resulting in the impedance bandwidth and mutual coupling improvements. Therefore, a -10 dB impedance bandwidth of 18.3% in the frequency range of 227.5-273.3 GHz is achieved for the modeled structure without employing a fixture. Fig. 7 shows the simulated radiation efficiency of the DRA for the two different configurations of (2x1y) and (2x3y). The average radiation efficiency of the DRA with (2x1y) configuration is about 91% and that of the DRA with (2x3y) configuration is about 93.6%. Hence, the improvement obtained is not noticeable on the average radiation efficiency.

III. RESULTS AND DISCUSSION

In this section, the fabricated prototype and the mechanical fixture designed for connecting the antenna to the VDI extenders are presented. Additionally, in order to demonstrate the performance of the presented DRA, an examination of the radiation characteristics of the fabricated prototype, including impedance matching, mutual coupling, gain, and radiation patterns is carried out. To make an appropriate comparison, the whole structure with the fixture is used to extract the simulation results. The S-parameters are measured using an Agilent Network Analyzer (PNA-X N5247A) and the radiation patterns are measured with the NSI near/far field system at our Poly-Grames research center, Polytechnique Montréal, University of Montreal.

A. PROTOTYPE FABRICATION

The presented and discussed dual-element DRA is manufactured. Fig. 8 depicts the geometry of the designed dual-element DRA (2x3y configuration) and photographs of

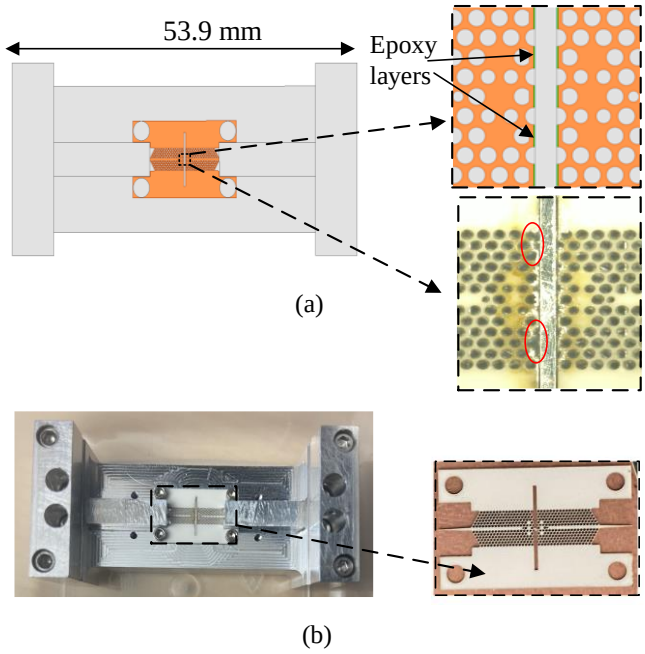

FIGURE 8. (a) Designed dual-element DRA, and (b) Photographs of the proposed back-to- back prototype.

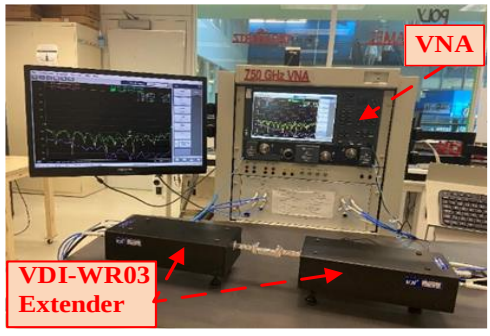

FIGURE 9. THz measurement set-up.

This work is licensed under a Creative Commons Attribution-NonCommercial-NoDerivatives 4.0 License. For more information, see https://creativecommons.org/licenses/by-nc-nd/4

This article has been accepted for publication in IEEE Open Journal of Antennas and Propagation. This is the author's version which has not been fully edited and content may change prior to final publication. Citation information: DOI 10.1109/OJAP.2024.3392628

the prototype. A larger slot is cut on the alumina layer to assemble the structure, resulting in an air gap creation between the central wall and the alumina waveguide. To mitigate the effect of air gap region, an epoxy layer is employed on both sides of the aluminium wall. In addition, metal screws are employed to ensure stability and prevent any unwanted air gap between layers, namely alumina layer, RO4003 supporting layer, and aluminium ground of the designed fixture. A new mechanical fixture was designed to measure the S-parameters and radiation patterns of the proposed antenna. The fixture connects the designed structure to WR3 VDI frequency extenders. WR3 rectangular waveguides are extended to minimize the impact of the fixture size as a scatterer on the radiation pattern of antenna.

B. MEASURED AND SIMULATED RESULTS

The S-parameters of the proposed dual-element DRA are measured and compared with the obtained simulation results in the frequency range of 220-280 GHz. The simulation is performed through CST Microwave Studio v2021. The THz measurement system setup and the proposed antenna under test (AUT) are shown in Fig. 9. The antenna is connected to the measurement setup (VDI extenders) through the fixture designed for this purpose.

The measured and simulated S-parameters of the whole structure with the fixture are shown in Fig. 10. From Fig. 10(a), the measurement results indicate proper reflection coefficient values and confirm the simulation results. The impedance bandwidth is about 17.01 % from 234.5 to 278.1 GHz in measurements as compared to that of 19.59% from 224.6 to 273.4 GHz in simulations for the prototype shown in Fig. 8. It is observed that there is a slight difference in measured reflection coefficients at two ports (port 1 and port 2) due to the fabrication errors. As shown in Fig. 10(b), the measured and simulated S_{21} and S_{12} parameter values are low due to the aluminium wall, as expected. The difference between the measured and simulated results are associated to additional losses of the fabricated prototype and feeding metallic waveguide used for the measurement.

To investigate the radiation patterns of the designed structure, the fabricated prototype was tested using NSI near/far field system at the Poly-Grames Research Center. Since there are only two VDI- WR3 extenders for a measurement at the frequency range of 220-280 GHz, one of them (VDI-WR3 extender) was employed and connected to the standard horn antenna (SHA) in the receiver side (RX). First, the measured and simulated radiation patterns are compared with each other when port 1 of the prototype is connected to the VDI extender and port 2 is connected to a matching load, and vice versa. Then the measured radiation patterns are combined using MATLAB.

Fig. 11 shows radiation pattern measurement setups. As can be seen, the system's measurement range is limited to -30° to 210° in the *XZ* plane and -90° to 90° in the *YZ* plane due to the system security boundaries (red color frame obstacles seen on the system) and the rotation range of the system arm of the

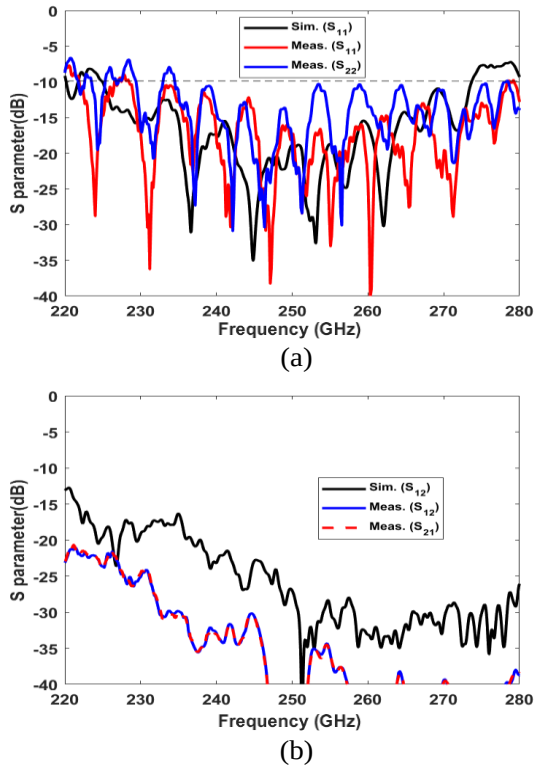

FIGURE 10. Simulated and measured (a) reflection coefficient for each port and (b) mutual coupling between ports for the proposed antenna in the presence of the aluminium wall.

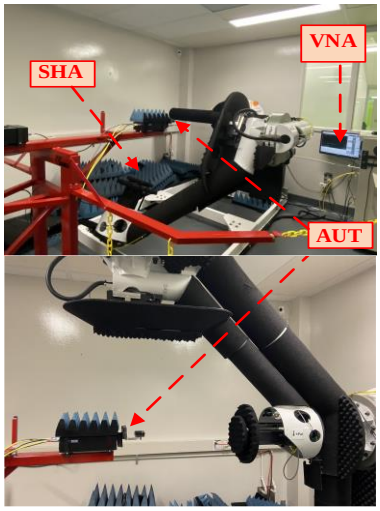

FIGURE 11. Radiation pattern measurement setups of the designed antenna.

standard horn antenna (SHA) in the receiver side (RX). Fig.12 shows the normalized co-polarization (Co-pol) and cross-polarization (X-pol) radiation patterns for the two ports of the designed DRA in the *XZ* and *YZ* planes at the frequencies of 247 GHz, 257 GHz, and 267 GHz. The high side lobe level and ripples on the radiation patterns, shown in Fig. 12 (a) to (c), can be attributed to the aluminum fixture and central wall in this direction (*XZ* plane) acting as a scatterer. Additionally, more ripples are observed on the measured copolar radiation

This work is licensed under a Creative Commons Attribution-NonCommercial-NoDerivatives 4.0 License. For more information, see https://creativecommons.org/licenses/by-nc-nd/4

This article has been accepted for publication in IEEE Open Journal of Antennas and Propagation. This is the author's version which has not been fully edited and content may change prior to final publication. Citation information: DOI 10.1109/OJAP.2024.3392628

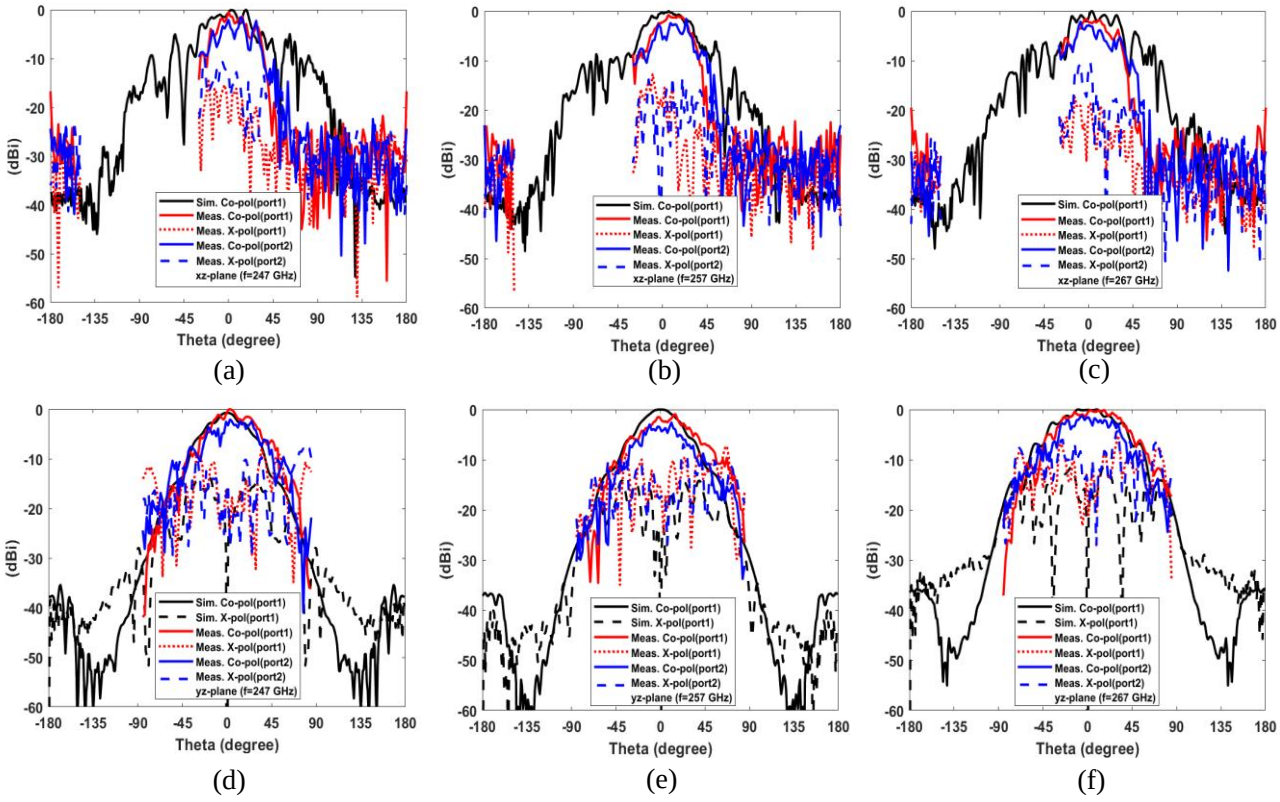

FIGURE 12. Normalized Co-pol and X-pol radiation patterns of the designed DRA for three different frequencies (a) E-plane 247 GHz, (b) E-plane 257 GHz, (c) E-plane 267 GHz, (d) H-plane 247 GHz, (e) H-plane 257 GHz, and (f) H-plane 267 GHz in the *XZ* and *YZ* planes.

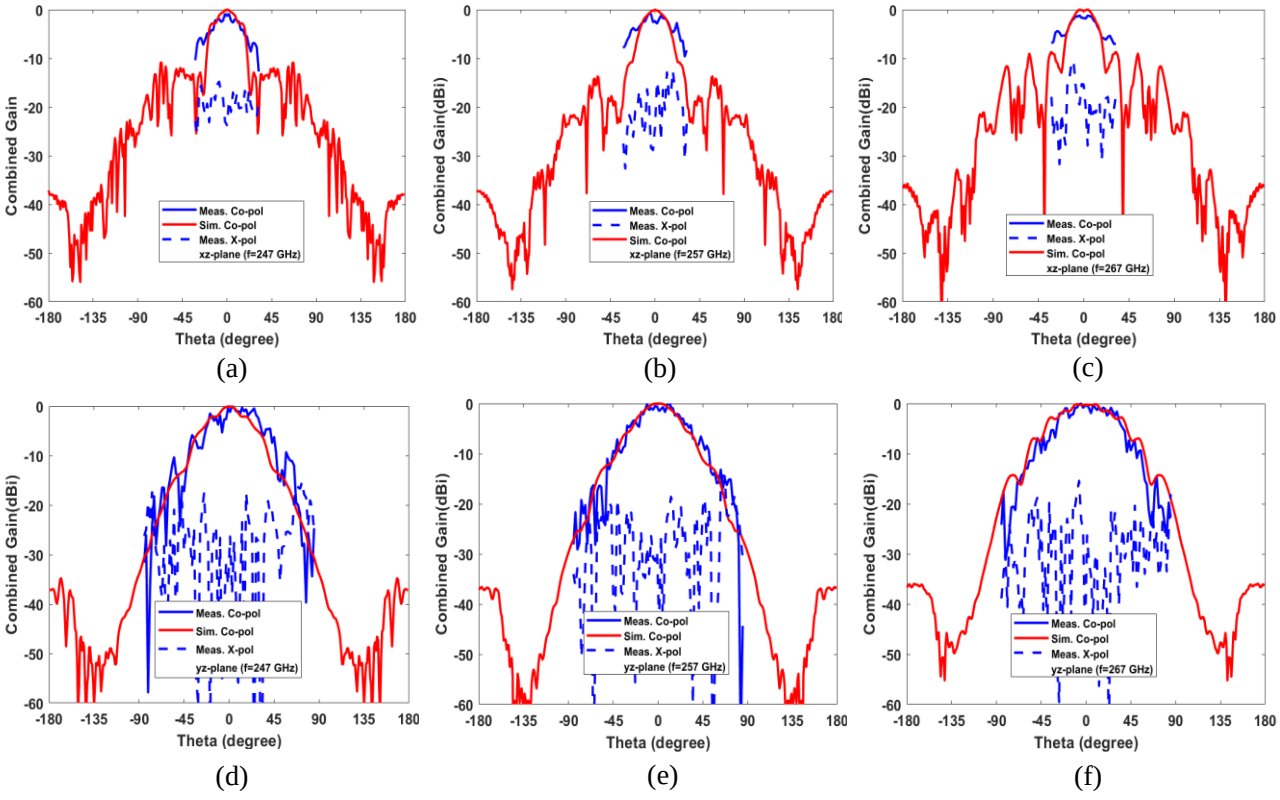

FIGURE 13. Normalized combined simulation and measured Co-pol and X-pol radiation patterns of the designed DRA for various frequencies: (a) E-plane 247 GHz, (b) E-plane 257 GHz, (c) E-plane 267 GHz, (d) H-plane 247 GHz, (e) H-plane 257 GHz, and (f) H-plane 267 GHz in the *XZ* and *YZ* planes.

This work is licensed under a Creative Commons Attribution-NonCommercial-NoDerivatives 4.0 License. For more information, see https://creativecommons.org/licenses/by-nc-nd/4

This article has been accepted for publication in IEEE Open Journal of Antennas and Propagation. This is the author's version which has not been fully edited and content may change prior to final publication. Citation information: DOI 10.1109/OJAP.2024.3392628

patterns of port2 in the main lobe direction compared to port 1, which can be attributed to the imperfect fabrication and the merging of a few air holes shown in Fig. 8(a) during the fabrication process of the designed alumina waveguide excited by port 2.

The combined co-polarization (Co-pol) and cross polarization (X-pol) radiation patterns extracted from measured and simulated results are illustrated in Fig. 13 in the *XZ* and *YZ* planes at three different frequencies, i.e., 247 GHz, 257 GHz, and 267 GHz. The co-polarization simulated results demonstrate that the side-lobe levels are less than -10 dB at all frequencies. The obtained normalized simulation results show cross-polarization levels less than -60 dBi. The normalized measured corresponding cross-polarization levels are less than – 15. 38 dBi in the boresight direction. It should be noted that the system arm could only handle measurements from -30° to 210° in the *XZ* plane. Therefore, the combined radiation patterns of two ports cannot be extracted from -150° to -30° and from 30° to 150°. Therefore, the measured combined radiation patterns are shown from -30° to 30° in Fig. 13.

The measured gain in the boresight direction versus frequency is depicted in Fig. 14 (a) for each port. The fabrication errors such as a few merged air holes shown in Fig. 8(a) can be the reason for the difference between the measured gains for each port. Additionally, the measured and simulated combined gain (dBi) are shown in Fig. 14 (b). The ripples and fluctuations on the combined measured patterns shown in Fig. 14 (b) can be attributed to the fluctuations on the measured radiation pattern of the port 2 shown in Fig 14 (a) which are resulted from the fabrication errors shown in Fig. 8(a). From these figures, it can be seen that the measured results confirm the simulated results. Additionally, the maximum value of measured gain in this direction (boresight direction) is about 16.08 dBi at the frequency of 243 GHz. The difference between the simulation and measurement levels can be attributed to alignment errors in the measurement setup.

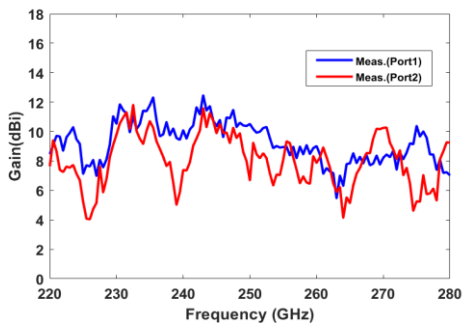

(a)

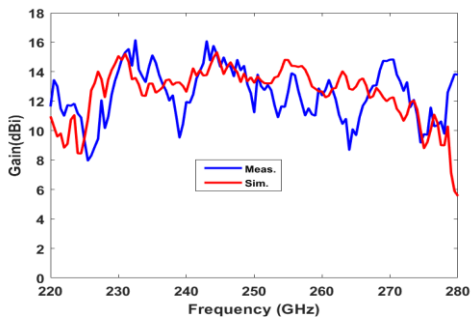

(b)

FIGURE 14. (a) Measured gain (dBi) in the boresight direction as a function of frequency for each port (port 1 and port 2), (b) Measured and simulated combined gain (dBi) in the boresight direction as a function of frequency.

TABLE 2. Comparison between current and previous works in the sub-THz/THz bands

Ref.	Frequency Band (GHz)	BW (%)	Realized Gain/ Gain(dBi)	Size (λ_0)	Antenna Type
[34]	186-205.5	9.96%	---	3.33e-4×2.122e-4	Nano DRA
[25]	110–130	-	16	0.32× 0.8× 0.2	Tapered antenna
[28]	1483-1535	3.46%	7.4	0.6× 0.25	DRA fed by photonic crystal waveguide
[35]	132	9.9%	8.2	0.286× 0.167 ×0.57	On-chip DRA (4×1 array)
[36]	311-331	6%	10.6	0.687× 0.214	DRA fed by photonic crystal waveguide
[20]	327	7.3%	6.7	0.327× 0.436× 0.545	On-chip antenna
This work	**234.5 to 278.1**	**17.01%**	**16.08**	**0.282× 0.217**	**Dual-element DRA-fed by the proposed waveguide**

λ_0: free space wavelength at the center frequency

Table 2 illustrates a comparative analysis of the proposed antenna with previous works on antenna designs operating in the Sub-THz and THz regimes. From this table, it appears that the proposed antenna can provide superior performance in terms of gain and impedance bandwidth.

IV. CONCLUSION

A fully embedded dual-element dielectric-based antenna directly fed by substrate integrated insulated guide was proposed and demonstrated in the frequency range of 220-280 GHz. A high radiation efficiency of about 93.6% was achieved. The developed prototype was fabricated and tested. The measured results exhibit an impedance bandwidth of about 17.01% over 234.5 to 278.1 GHz and a maximum gain of 16.08 dBi in broadside direction that validate the simulation results. These characteristics make the proposed antenna suitable for short-range wireless communication applications, imaging, and sensing, in the Sub- and THz regime.

ACKNOWLEDGMENT

This work was partially funded by the Natural Sciences and Engineering Research Council of Canada (NSERC), under the New Frontiers in Research Fund (NFRF) with project number NFRFE-2020-00355.

This work is licensed under a Creative Commons Attribution-NonCommercial-NoDerivatives 4.0 License. For more information, see https://creativecommons.org/licenses/by-nc-nd/4

REFERENCES

[1] M. Z. Chowdhury, M. Shahjalal, S. Ahmed and Y. M. Jang, "6G wireless communication systems: applications, requirements, technologies, challenges, and research directions," in *IEEE Open J. Comm. Soc.*, vol. 1, pp. 957-975, 2020.

[2] Y. Xing and T. S. Rappaport, "Terahertz wireless communications: co-sharing for terrestrial and satellite systems above 100 GHz," in *IEEE Commun. Lett.*, vol. 25, no. 10, pp. 3156-3160, Oct. 2021.

[3] T. S. Rappaport et al., "Wireless communications and applications above 100 GHz: opportunities and challenges for 6G and beyond," in *IEEE Access*, vol. 7, pp. 78729-78757, June 2019.

[4] Y. Shang, H. Yu, H. Fu and W. M. Lim, "A 239–281 GHz CMOS receiver with on-chip circular-polarized substrate integrated waveguide antenna for sub-terahertz imaging," in *IEEE Trans Terahertz Sci Technol.*, vol. 4, no. 6, pp. 686-695, Nov. 2014.

[5] D. Seo, H. Kim, S. Oh, J. Kim and J. Oh, "Ultrathin high-gain D-band transmitarray based on a spatial filter topology utilizing bonding layer effect," in *IEEE Antennas Wireless Propag. Lett.*, vol. 21, no. 10, pp. 1945-1949, Oct. 2022.

[6] H. Shams, M. J. Fice, L. Gonzalez-Guerrero, C. C. Renaud, F. van Dijk and A. J. Seeds, "Sub-THz wireless over fiber for frequency band 220–280 GHz, " in *J. Lightwave Technol.*, vol. 34, no. 20, pp. 4786-4793, 15 Oct.15, 2016.

[7] T. Li, A. Bhutani and T. Zwick, "A D-band corporate-feed gap-cavity slot array antenna using virtual PEC method," in *IEEE Trans. Antennas Propag.* , vol. 70, no. 8, pp. 7258-7263, Aug. 2022.

[8] B. Aqlan, M. Himdi, H. Vettikalladi and L. Le-Coq, "A circularly polarized sub-terahertz antenna with low-profile and high-gain for 6G wireless communication systems," in *IEEE Access*, vol. 9, pp. 122607-122617, 2021.

[9] T. Tajima, H. -J. Song, K. Ajito, M. Yaita and N. Kukutsu, "300-GHz step-profiled corrugated horn antennas integrated in LTCC," in *IEEE Trans. Antennas Propag.* , vol. 62, no. 11, pp. 5437-5444, Nov. 2014.

[10] N. Llombart, G. Chattopadhyay, A. Skalare and I. Mehdi, "Novel terahertz antenna based on a silicon lens fed by a leaky wave enhanced waveguide," in *IEEE Trans. Antennas Propag.* , vol. 59, no. 6, pp. 2160-2168, June 2011.

[11] S. -W. Qu, H. Yi, B. J. Chen, K. B. Ng and C. H. Chan, "Terahertz reflecting and transmitting metasurfaces," in *Proc. IEEE*, vol. 105, no. 6, pp. 1166-1184, June 2017.

[12] E. Rahmati, M. Ahmadi-Boroujeni, "Improving the efficiency and directivity of THz photoconductive antennas by using a defective photonic crystal substrate," *Opt. Commun.* 412 pp. 74–79, 2018.

[13] E. Rahmati and M. Ahmadi-Boroujeni, "Design of terahertz photoconductive antenna arrays based on defective photonic crystal substrates," *Opt. Laser Technol.* 114, pp. 89–94, 2019.

[14] Q. -Y. Guo and H. Wong, "155 GHz dual-polarized Fabry–Perot cavity antenna using LTCC-based feeding source and phase-shifting surface," in *IEEE Trans. Antennas Propag.* , vol. 69, no. 4, pp. 2347-2352, April 2021.

[15] S. -Y. Zhu, Y. -L. Li, K. -M. Luk and S. W. Pang, "Compact high-gain Si-Imprinted THz antenna for ultrahigh speed wireless communications," in *IEEE Trans. Antennas Propag.* , vol. 68, no. 8, pp. 5945-5954, Aug. 2020.

[16] H. Chu, Y. -X. Guo, T. -G. Lim, Y. M. Khoo and X. Shi, "135-GHz micromachined on-chip antenna and antenna array," *IEEE Trans. Antennas Propag.* , vol. 60, no. 10, pp. 4582-4588, Oct. 2012.

[17] S. N. Nallandhigal, P. Burasa and K. Wu, "Deep integration and topological cohabitation of active circuits and antennas for power amplification and radiation in standard CMOS," in *IEEE Trans. Microw. Theory Techn*, vol. 68, no. 10, pp. 4405-4423, Oct. 2020.

[18] A. Petosa, "*Dielectric Resonator Antenna Handbook*," Norwood, MA, USA: Artech House, 2007

[19] E. Rahmati and M. S. Sharawi,"Design of a Sub-THz Dielectric Resonator Antenna Fed by Substrate Integrated Image Guide (SIIG) Technology," 2023 *IEEE International Symposium on Antennas and Propagation and USNC-URSI Radio Science Meeting* (USNC-URSI), Portland, OR, USA, 2023, pp. 1165-1166.

[20] C. -H. Li and T. -Y. Chiu, " 340-GHz low-cost and high-gain on-chip higher order mode dielectric resonator antenna for THz applications," in *IEEE Trans Terahertz Sci Technol* , vol. 7, no. 3, pp. 284-294, May 2017.

[21] P. V. Bijumon, Y. M. M. Antar, A. P. Freundorfer and M. Sayer, "Dielectric resonator antenna on silicon substrate for system on-chip applications," in *IEEE Trans. Antennas Propag.* , vol. 56, no. 11, pp. 3404-3410, Nov. 2008.

[22] A. Patrovsky and K. Wu, "94-GHz planar dielectric rod antenna with substrate integrated image guide (SIIG) feeding," in *IEEE Antennas Wireless Propag. Lett.*, vol. 5, pp. 435-437, 2006.

[23] M. Bozzi, A. Georgiadis, K. Wu, "Review of substrate-integrated waveguide circuits and antennas," *IET Microw. Antennas Propag.*, 5, (8), pp. 909-920, 2011.

[24] A. Mahmoud, J. Ruiz-García, O. de Sagazan, M. Ettorre, R. Sauleau and D. González-Ovejero, "Low-cost and low-profile sub-terahertz Luneburg lens beamformer on polymer," in *IEEE Antennas Wireless Propag. Lett.*, vol. 22, no. 6, pp. 1411-1415, June 2023.

[25] N. Ranjkesh, A. Taeb, N. Ghafarian, S. Gigoyan, M. A. Basha and S. Safavi-Naeini, "Millimeter-wave suspended silicon-on-glass tapered antenna with dual-mode operation," in *IEEE Trans. Antennas Propag.* , vol. 63, no. 12, pp. 5363-5371, Dec. 2015.

[26] A. Patrovsky and K. Wu, "Substrate integrated image guide array Antenna for the upper millimeter-wave spectrum," in *IEEE Trans. Antennas Propag.* , vol. 55, no. 11, pp. 2994-3001, Nov. 2007.

[27] M. Tajik and N. Granpayeh, "Dielectric resonator antenna fed by photonic crystal waveguide based on silicon-on-glass technology," *Opt Eng*, vol. 59, no. 11, Nov 2020, Artn 117107.

[28] Y. Zhou, R. Li, P. Jiang, X. Guo, and S. Li, "Design of high efficiency cylindrical dielectric resonator antenna based on topological photonic crystals," *J. Appl. Phys.* , vol. 133, no. 8, 2023.

[29] Y. -X. Sun and K. W. Leung, "Circularly polarized substrate-integrated cylindrical dielectric resonator antenna array for 60 GHz applications," in *IEEE Antennas Wireless Propag. Lett.*, vol. 17, no. 8, pp. 1401-1405, Aug. 2018.

[30] K. Gong and X. H. Hu, "Low-profile substrate integrated dielectric resonator antenna implemented with PCB process," in *IEEE Antennas Wireless Propag. Lett.*, vol. 13, pp. 1023-1026, 2014.

[31] A. Patrovsky and K. Wu, "Substrate integrated image guide (SIIG)-a planar dielectric waveguide technology for millimeter-wave applications," in *IEEE Trans. Microw. Theory Techn*, vol. 54, no. 6, pp. 2872-2879, June 2006.

[32] N. Dolatsha and J. Hesselbarth, "Propagation and excitation of the higher-order E_x^{11} mode in an insulated image guide," *Microw. Opt. Technol. Lett.*, vol. 54, no. 1, pp. 179-181, 2012.

[33] *N. Dolatsha and J. Hesselbarth,* "*Millimeter-wave antenna array fed by an insulated image guide operating in Higher-Order Ex^{11} Mode*," *in IEEE Trans. Antennas Propag., vol. 61, no. 6, pp. 3369-3373, June 2013.*

[34] AG. N. Malheiros-Silveira, G. S. Wiederhecker, and H. E. Hernandez-Figueroa, "Dielectric resonator antenna for applications in nanophotonics," *Opt Express*, vol. 21, no. 1, pp. 1234- 9, Jan. 2013.

[35] D. B. Hou, W. Hong, J. X. Chen, Z. Song, P. P. Yan, and Y. Z. Xiong, "130 GHz on-chip dielectric resonator antenna array in CMOS technology," *Proc. 6th Asia-Pac. Conf. Antennas Propag. (APCAP), 2017*.

[36] W. Withayachumnankul, R. Yamada, C. Fumeaux, M. Fujita, and T. Nagatsuma, "All-dielectric integration of dielectric resonator antenna and photonic crystal waveguide," *Opt Express*, vol. 25, no. 13, pp. 14706- 14714, June 2017, doi: 10.1364/OE.25.014706.

Ehsan Rahmati (Member, IEEE) received the M.Sc. degree in electrical engineering from the University of Montreal (École Polytechnique de Montréal), Montreal, QC, Canada, in 2023.
He was also a member of the Poly-Grames Research Center. His research interests include RF, millimeter-wave and terahertz (THz) designs, antenna-in-package, RFIC and Integrated circuit technology. He was the recipient of Bourse d'excellence CAE - R. Fraser-Elliott maitrise in 2023 and Roland and Isabelle Bureau excellence scholarship in 2022.

This work is licensed under a Creative Commons Attribution-NonCommercial-NoDerivatives 4.0 License. For more information, see https://creativecommons.org/licenses/by-nc-nd/4

This article has been accepted for publication in IEEE Open Journal of Antennas and Propagation. This is the author's version which has not been fully edited and content may change prior to final publication. Citation information: DOI 10.1109/OJAP.2024.3392628

Pascal Burasa (Member, IEEE) received the B.Eng., M.A.Sc., and Ph.D. degrees (Hons.) in electrical engineering from the École Polytechnique de Montréal (University of Montreal), Montreal, QC, Canada, in 2006, 2008, and 2016, respectively. From 2008 to 2010, he was with the Microelectronic Research Group, École Polytechnique de Montréal, where he developed CMOS color image sensors free of optic filters. He is currently a Researcher with the Poly-Grames Research Center, École Polytechnique de Montréal. He has authored or coauthored several peer-reviewed journal articles and conference papers. He holds several patents. His research interests include microelectronic circuits and systems operating at millimeter-wave and terahertz (THz) frequencies for radar, imaging, wireless sensing, and ultrahigh-speed communication applications, including millimeter-wave/terahertz reconfigurable transceiver architectures and components for multifunction wireless systems.

The Dr. Burasa has served as a Reviewer for the IEEE TRANSACTIONS ON MICROWAVE THEORY AND TECHNIQUES, the IEEE TRANSACTIONS ON TERAHERTZ SCIENCE AND TECHNOLOGY, the IEEE TRANSACTIONS ON ANTENNAS AND PROPAGATION, the IEEE TRANSACTIONS ON CIRCUITS AND SYSTEMS—I: REGULAR PAPERS, IEEE MICROWAVE AND WIRELESS COMPONENTS LETTERS.

Elham Baladi (Member, IEEE) received the B.Sc. degree in electrical engineering–telecommunications from the Iran University of Science and Technology, Tehran, Iran, in 2013, and the Ph.D. degree in electromagnetics and microwaves from the University of Alberta, Edmonton, AB, Canada, in January 2019. She developed a novel class of resonant metasurfaces during her Ph.D. degree and investigated their applications for shielding, imaging, and selective transmission.

Dr. Baladi was a postdoctoral fellow with the University of Toronto, Toronto, ON, Canada, from February 2019 to February 2021, where she conducted research on the modeling and development of reconfigurable antenna arrays for Space applications. She was an Antenna and RF Filter Design Engineer with Syntronic Research and Development Canada, Ottawa, ON, Canada, from February 2021 to August 2022, where she worked on the development of RF cavity filters, duplexers, and multi-band antennas for 5G, IoT, and wireless communication systems. Dr. Baladi joined the Electrical Engineering department of Polytechnique Montreal, Montreal, QC, Canada, as an Assistant Professor in September 2022. Her research interests include the development of novel multi-band multi-beam antenna arrays, metasurfaces, reconfigurable intelligent surfaces, microwave sensors, and radar imaging technologies.

The Dr. Baladi was the recipient of the University of Alberta Doctoral Recruitment scholarship, the Alberta Innovates Technology Futures scholarship, the IEEE AP-S Doctoral Research Award, and two honorable mention awards in the student-paper competitions of the 2016 and 2017 IEEE AP-S Symposia. She has been a lecturer at York University (Winter 2020) and the University of Alberta (Winter 2017) and serves as a Reviewer for multiple IEEE and OSA journals. She also currently serves as the chair of the IEEE Antenna & Propagation Section and Vice-Chair of IEEE Women in Engineering in Montreal.

Mohammad S. Sharawi (Fellow, IEEE) is currently a Lead Engineer at Blue Origin LLC working on research and development projects for space communication systems. He was a Full tenured Professor (Professeur titulaire) of electrical engineering with Polytechnique Montréal, Montreal, QC, Canada between 2019-2023. Dr. Sharawi was with King Fahd University of Petroleum and Minerals, Dhahran, Saudi Arabia, from 2009 to 2018, where he founded and directed the Antennas and Microwave Structure Design Laboratory (AMSDL). He was a Visiting Professor with the Intelligent Radio Laboratory (iRadio), Department of Electrical Engineering, University of Calgary, Calgary, AB, Canada, in summer, fall 2014. He was a Visiting Research Professor with Oakland University, Rochester, MI, USA, during 2023 and in 2013. Dr. Sharawi has more than 400 papers published in refereed journals and international conferences, 11 book chapters (two of which in the Antenna Handbook, fifth edition, McGraw Hill, 2018), one single authored book titled Printed MIMO Antenna Engineering (Artech House, 2014), the Lead Author of the book Design and Applications of Active Integrated Antennas (Artech House, 2018), and a co-author of the upcoming book MIMO Antenna Systems for 5G and Beyond (IEEE-Wiley, 2024). He has 28 issued/granted and ten pending patents in the U.S. Patent Office. His research interests include multiband printed multiple-input–multiple-output (MIMO) antenna systems, reconfigurable and active integrated antennas, millimeter-wave antennas, integrated 4G/5G and beyond 5G antenna systems, shared aperture and encapsulated antennas, microwave sensors, applied electromagnetics, sub-THz structures, and computational methods. He received his MSc. and PhD. degrees from Oakland University, Michigan, USA, in 2002 and 2006, respectively.

Dr. Sharawi was a recipient of the Abdul Hameed Shoman Foundation Award for Arab Researchers for the category of wireless systems in 2020 in addition to various best IEEE conference paper awards. He has served on the Technical and Organizational Program Committees as well as organized several special sessions on MIMO antenna systems and their applications in 4G and 5G wireless systems in several international conferences, such as European Conference on Antennas and Propagation (EuCAP), Antennas and Propagation Society (APS), International Microwave Workshop Series on 5G Hardware and System Technologies (IMWS-5G), Asia-Pacific Conference on Antennas and Propagation (APCAP), International Workshop on Antenna Technology (iWAT), among many others for many years. He has served as the IEEE APS Chair for the Montreal Section (2020–2023) and an Active Member for the IEEE Member Benefits Committee leading the initiative of the APS Student Travel Grant. He is also the Regional Delegate of the EuRAAP in North America until Dec. 2023. He was an Associate Editor of IEEE Antennas and Wireless Propagation Letters from 2019 to 2023. He was the Specialty Chief Editor of the newly launched Frontiers in Communications and Networks for the System and Test-Bed Design Section from 2020 to 2022. He is serving as an Associate Editor for the IEEE Open Journal of Antennas and Propagation and IET Microwaves, Antennas and Propagation (Wiley), and an Area Editor (antennas and microwave devices and systems) for Microwave and Optical Technology Letters (Wiley). He is a Distinguished Lecturer (DL) for APS for the period 2023–2025, a Fellow of the IEEE and IET.

This work is licensed under a Creative Commons Attribution-NonCommercial-NoDerivatives 4.0 License. For more information, see https://creativecommons.org/licenses/by-nc-nd/4